In: Understanding Density Matrices
Editor: N. V. Danielsen
ISBN: 978-1-53616-245-5

Chapter 6

DENSITY-MATRIX RENORMALIZATION-GROUP STUDY OF LATTICE GAS ON THE SURFACE OF A WURTZITE CRYSTAL STRUCTURE

Noriko Akutsu[1,*] ***and Yasuhiro Akutsu***[2]
[1]Faculty of Engineering, Osaka Electro-Communication University,
Hatsu-cho, Neyagawa, Osaka, Japan
[2]Department of Physics, Graduate School of Osaka University,
Machikaneyama, Toyonaka, Osaka, Japan

Abstract

Many semiconductors, such as CdI, InN, GaN, and AlN, have a wurtzite crystal structure. The surfaces of these crystals have been experimentally studied extensively, but there have not been sufficient theoretical studies of the surface thermodynamics of wurtzite crystal structures. In this article, we calculate the internal surface energy, specific heat of a lattice gas, and sub-lattice coverage of the lattice gas on the $(10\bar{1}0)$ surface of a wurtzite crystal structure using the product-wave-function renormalization-group (PWFRG) method (a tensor network method). The PWFRG method is a transfer matrix version of the density-matrix renormalization-group (DMRG) method. A characteristic feature of the present calculation is that the right density matrix is not the same as the

*Corresponding Author's Email: nori3@phys.osakac.ac.jp,

left density matrix due to the specific crystal symmetry of the wurtzite structure. The calculated results are compared with results obtained by the Monte Carlo method. We apply the results to the (0001) and $(10\bar{1}0)$ surfaces (interfaces) of Ih–ice. From the transition temperature of the lattice gas, the effective bond energies between molecules on the prism $((10\bar{1}0))$ surfaces are obtained as 71.8meV and 68.1meV for the ice/vapor and ice/water surfaces, respectively. The surface energies at $T = 0$ K of the ice/vapor surface $\gamma_{\rm surf}^{(0001)}$ and $\gamma_{\rm surf}^{(10\bar{1}0)}$ are obtained as 32.5 mJ/m^2 and 34.6 mJ/m^2, respectively, and the surface energies at $T = 0$ K of the ice/water surface $\gamma_{\rm surf}^{(0001)}$ and $\gamma_{\rm surf}^{(10\bar{1}0)}$ are obtained as 30.8 mJ/m^2 and 32.8 mJ/m^2.

PACS: 05.70.Np, 05.50.+q, 05.10-a, 83.80.Nb, 82.65.Dp, 68.35.Ct, 05.10.Cc, 68.35.Md

Keywords: density-matrix renormalization-group method, product wave-function renormalization-group method, tensor network method, two-dimensional Ising model with a uniform and a staggered field, Ih–ice, faceting transition temperature, roughening transition temperature, effective bond energy, surface energy of the basal and prism plane of ice

1. INTRODUCTION

Since it was first presented by White [1], the numerical renormalization-group method called the density-matrix renormalization-group (DMRG) method has become a powerful tool for reliably calculating one-dimensional (1D) quantum systems such as 1D quantum spin systems [2, 3]. Nishino, Okunishi, and their colleagues developed the product-wave-function renormalization-group (PWFRG) method, a variant of the DMRG method, for 2D classical systems [4, 5, 6]. The Hamiltonian in a 1D quantum system can be mapped to a transfer matrix in a 2D classical system using the Suzuki–Trotter formula [7].

This PWFRG method is useful for obtaining physical quantities on a crystal surface [8]–[22]. Since crystal surfaces and lattice gases are two-dimensional objects, thermal fluctuations are strong enough to destabilize their ordered state at finite temperatures [23]. Therefore, calculations based on the mean field approximation or the quasi-chemical approximation sometimes give incorrect results. More precise calculations than the mean field approximation are required to obtain reliable results on surfaces at finite temperatures.

In this context, the trimer–monomer transition on the Si(111) surface was studied using the PWFRG method [9]. The critical curves of the trimer–monomer mixtures calculated by the PWFRG method well describe the convergence of the critical curves to the exact critical temperature of the hard hexagon model. Adsorption with a coverage of less than 1 is shown to change the surface tension, causing thermal step bunching [10, 11, 12, 13]. Here, the surface tension is the surface free-energy per normal unit area. Detailed PWFRG calculations on a restricted solid-on-solid (RSOS) model with a point-contact-type step–step attraction (p-RSOS) model gives a discontinuous surface tension [14, 15, 16] at low temperatures. Based on the connectivity of the surface tension, a faceting diagram with respect to the step assembling/disassembling has been obtained [17]. This discontinuous surface tension provides new insights for macrostep formation at the equilibrium [18, 19, 20, 21], such as for SiC or for reaction- (interface-) limited steady state growth/recession [22] .

In this article, we outline the PWFRG method used to study surface phenomena. As a model, we consider a 2D lattice gas on the (0001) and the $(10\bar{1}0)$ surfaces of a wurtzite crystal structure. The sub-lattice coverage and the specific heat are calculated using the PWFRG method. The most characteristic feature of the calculation is that the right density matrix is not the same as the left density matrix due to the specific crystal symmetry of the wurtzite structure. We apply the results to the basal and prism planes of Ih–ice.

In §2 we explain the wurtzite crystal structure and its lattice gas model on the (0001) and $(10\bar{1}0)$ surfaces. In §3, the outline of the PWFRG method is explained. In §4, the calculated results are compared with the exact results and Monte Carlo results to demonstrate the accuracy of the PWFRG calculations. The application to Ih–ice is shown in §5. Discussions and the conclusion are given in §6 and §7.

2. TWO-DIMENSIONAL LATTICE GAS MODEL

2.1. Lattice Gas Hamiltonian

The wurtzite crystal structure is shown in Fig. 1. Many hexagonal II-VI and III-V semiconductors have this crystal structure. For the (0001) surface, the honeycomb lattice consists of two triangular sub-lattices, denoted by $\mathcal{A}'$ and $\mathcal{B}'$ (Fig. 2 (a)). For the $(10\bar{1}0)$ surface, the surface layer consists of four rectangular sub-lattices, denoted by $\mathcal{A}'$, $\mathcal{B}'$, $\mathcal{A}''$, and $\mathcal{B}''$ (Fig. 2 (b)).

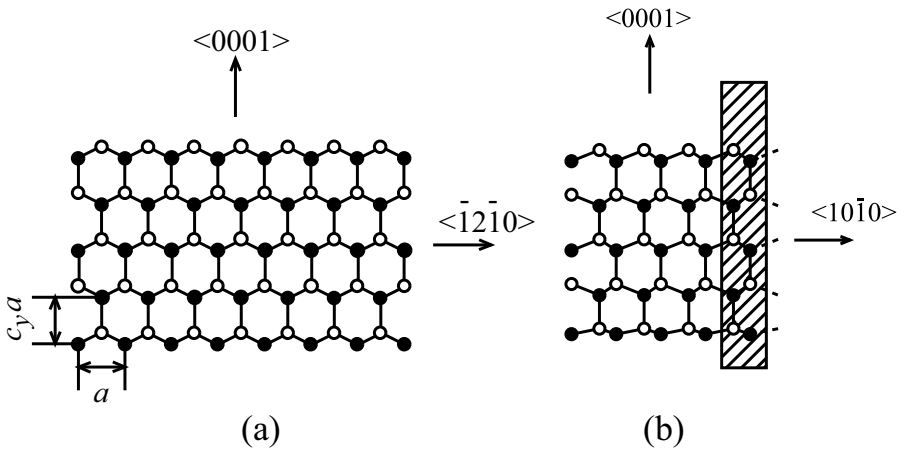

Figure 1. $(10\bar{1}0)$ surface of the wurtzite structure. The open and closed circles denote A atoms and B atoms for the two-component systems, respectively. (a) Overhead view. (b) Side view. The shaded area indicates the lattice gas layer.

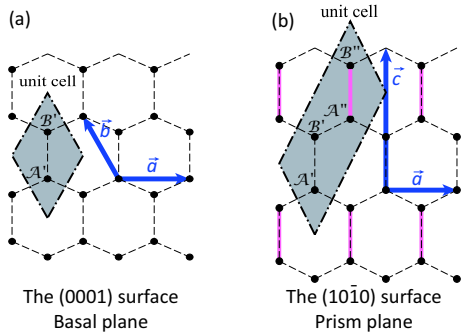

Figure 2. Overhead views of the (0001) and $(10\bar{1}0)$ surfaces of the wurtzite crystal structure. The dark thick arrows denote the lattice vectors $\vec{a}$, $\vec{b}$, and $\vec{c}$. (a) Basal plane. The triangular sub-lattices are denoted by $\mathcal{A}'$ and $\mathcal{B}'$. (b) Prism plane. The elongated triangular sub-lattices are denoted by $\mathcal{A}'$, $\mathcal{B}'$, $\mathcal{A}''$, and $\mathcal{B}''$. The thick light-colored bonds are outer bonds parallel to the $(10\bar{1}0)$ plane (Fig. 1 (b)).

We consider the surface energy by counting the number of broken bonds for a surface configuration. The lateral bond energy is denoted by ϕ. Then, the

2D lattice gas Hamiltonian for the (0001) surface (basal plane) is expressed as follows [24, 25, 26, 27]:

$$\begin{aligned}\mathcal{H}_{\mathrm{LG,b}} &= -\phi \sum_{(\vec{x})} \Big[C_{\mathcal{A}'}(\vec{x}) C_{\mathcal{B}'}(\vec{x}) + C_{\mathcal{A}'}(\vec{x}) C_{\mathcal{B}'}(\vec{x} - \vec{b}) \\ &\quad + C_{\mathcal{A}'}(\vec{x}) C_{\mathcal{B}'}(\vec{x} - \vec{b} - \vec{a}) \Big] \\ &\quad - \epsilon_{\mathcal{A}'} \sum_{\vec{x}} C_{\mathcal{A}'}(\vec{x}) - \epsilon_{\mathcal{B}'} \sum_{\vec{x}} C_{\mathcal{B}'}(\vec{x}), \end{aligned} \tag{1}$$

where $\epsilon_{\mathcal{A}'}$ and $\epsilon_{\mathcal{B}'}$ are the surface chemical potentials for lattice gas particles on the $\mathcal{A}'$ sub-lattice and $\mathcal{B}'$ sub-lattice, and $C_{\mathcal{A}'}(\vec{x}) = \{0, 1\}$ is the lattice gas variable at a lattice site $\vec{x}$ on the sub-lattice $\mathcal{A}'$. When $C_{\mathcal{A}'}(\vec{x}) = 1$, the sub-lattice site $\mathcal{A}'$ at the lattice point $\vec{x}$ is occupied, whereas for $C_{\mathcal{A}'}(\vec{x}) = 0$ it is empty. Similarly, $C_{\mathcal{B}'}(\vec{x})$ is assigned for a particle on the $\mathcal{B}'$ sub-lattice site.

For the $(10\bar{1}0)$ surface (the prism plane), the 2D lattice gas Hamiltonian is expressed as follows [28]:

$$\begin{aligned}\mathcal{H}_{\mathrm{LG,p}} &= -\phi \sum_{(\vec{x})} [C_{\mathcal{A}'}(\vec{x}) C_{\mathcal{B}'}(\vec{x}) + C_{\mathcal{A}'}(\vec{x}) C_{\mathcal{B}''}(\vec{x} - \vec{c}) \\ &\quad + C_{\mathcal{A}'}(\vec{x}) C_{\mathcal{B}''}(\vec{x} - \vec{a} - \vec{c}) + C_{\mathcal{A}''}(\vec{x}) C_{\mathcal{B}'}(\vec{x}) \\ &\quad + C_{\mathcal{A}''}(\vec{x}) C_{\mathcal{B}''}(\vec{x}) + C_{\mathcal{A}''}(\vec{x}) C_{\mathcal{B}'}(\vec{x} + \vec{a})] \\ &\quad - \epsilon_{\mathcal{A}'} \sum_{\vec{x}} C_{\mathcal{A}'}(\vec{x}) - \epsilon_{\mathcal{B}'} \sum_{\vec{x}} C_{\mathcal{B}'}(\vec{x}) - \epsilon_{\mathcal{A}''} \sum_{\vec{x}} C_{\mathcal{A}''}(\vec{x}) \\ &\quad - \epsilon_{\mathcal{B}''} \sum_{\vec{x}} C_{\mathcal{B}''}(\vec{x}). \end{aligned} \tag{2}$$

2.2. Thermodynamics of Stoichiometrically Binary Systems [24]

Let $\mu_{\mathrm{A,crys}}(T)$ be the bulk chemical potential of A-atoms in the crystal, neglecting the pressure dependence of $\mu_{\mathrm{A,crys}}(T)$. $\mu_{\mathrm{A,gas}}(P_{\mathrm{A}}, P_{\mathrm{B}}, T)$ is the bulk chemical potential of A-atoms in the ambient gas. P_{A} is the partial pressure of A-atoms in the bulk gas phase. Similarly, $\mu_{\mathrm{B,crys}}(T)$, $\mu_{\mathrm{B,gas}}(P_{\mathrm{A}}, P_{\mathrm{B}}, T)$, and P_{B} are defined for B-atoms. At the equilibrium for the coexistence of the two phases, the condition

$$\mu_{\mathrm{A,gas}}(P_{\mathrm{A}}, P_{\mathrm{B}}, T) + \mu_{\mathrm{B,gas}}(P_{\mathrm{A}}, P_{\mathrm{B}}, T) = \mu_{\mathrm{A,crys}}(T) + \mu_{\mathrm{B,crys}}(T) \tag{3}$$

should be satisfied [24, 28, 29].

Moreover, we assume the following relationships:

$$\begin{aligned}
\mu_{\mathrm{A,gas}}(P_{\mathrm{A}}, P_{\mathrm{B}}, T) &= k_{\mathrm{B}}T \ln[P_{\mathrm{A}}] + \mathrm{const}, \\
\mu_{\mathrm{B,gas}}(P_{\mathrm{A}}, P_{\mathrm{B}}, T) &= k_{\mathrm{B}}T \ln[P_{\mathrm{B}}] + \mathrm{const}', \\
\mu_{\mathrm{A,crys}}(T) &= k_{\mathrm{B}}T \ln[P_{0\mathrm{A}}] + \mathrm{const}, \\
\mu_{\mathrm{B,crys}}(T) &= k_{\mathrm{B}}T \ln[P_{0\mathrm{B}}] + \mathrm{const}'.
\end{aligned} \tag{4}$$

To simplify the description, we introduce a relative chemical potential $\Delta\mu_A$, defined by

$$\begin{aligned}
\Delta\mu_A &= \mu_{\mathrm{A,gas}}(P_{\mathrm{A}}, P_{\mathrm{B}}, T) - \mu_{\mathrm{A,crys}}(T) \\
&= k_{\mathrm{B}}T \ln[P_{\mathrm{A}}/P_{0\mathrm{A}}].
\end{aligned} \tag{5}$$

From the phase coexistence condition Eq. (3), we obtain

$$\begin{aligned}
\Delta\mu_B &= [\mu_{\mathrm{B,gas}}(P_{\mathrm{A}}, P_{\mathrm{B}}, T) - \mu_{\mathrm{B,crys}}(T)] \\
&= k_{\mathrm{B}}T \ln[P_{\mathrm{B}}/P_{0\mathrm{B}}] \\
&= -\Delta\mu_A.
\end{aligned} \tag{6}$$

The physical meaning of $\Delta\mu_A$ is the bias between the components in the ambient gas phase. When the ambient phase of the crystal is a solution, the relative chemical potential can be applied by replacing the vapor pressures by the constituent concentrations in the ambient solution.

The surface chemical potential can also be calculated by simple broken bond counting. For the (0001) surface, the surface chemical potentials are expressed by

$$\epsilon_{\mathcal{A}'} = \Delta\mu_A + \Delta E_b - z\phi/2, \quad \epsilon_{\mathcal{B}'} = \Delta\mu_B - \Delta E_b - z\phi/2, \tag{7}$$

where $\Delta E_b \approx \phi/2$ is the half energy of a connected bond directed into the crystal and $z = 3$ is the number of nearest neighbor (nn) sites in the lateral plane. The particles at $\mathcal{B}'$-sites have dangling bonds protruding outward from the layer. The excess energy of the dangling bond is assumed to be ΔE_b. The third term in the right hand side denotes the excess energy of the broken bonds in the layer when a single particle exists.

Similarly, for the $(10\bar{1}0)$ surface, the surface chemical potentials are expressed by

$$\begin{aligned}
\epsilon_{\mathcal{A}'} &= \Delta\mu_A + \Delta E_p - z\phi/2, \quad \epsilon_{\mathcal{B}'} = \Delta\mu_B + \Delta E_p - z\phi/2, \\
\epsilon_{\mathcal{A}''} &= \Delta\mu_A - \Delta E_p - z\phi/2, \quad \epsilon_{\mathcal{B}''} = \Delta\mu_B - \Delta E_p - z\phi/2,
\end{aligned} \tag{8}$$

where $z = 3$ and ΔE_p is the energy gain for a bond inward to the crystal from a layer on the prism plane.

Interestingly, the lattice gas Hamiltonian on the prism plane (Eq. (2)) is equivalent to the lattice gas Hamiltonian on the basal plane (Eq. (1)), if we assume $\Delta\mu_A \to \Delta\mu_A + \Delta E_b$ and $\Delta E_p = 0$ in Eq. (8).

2.3. Mapping to the 2D nn Ising Anti-Ferromagnet

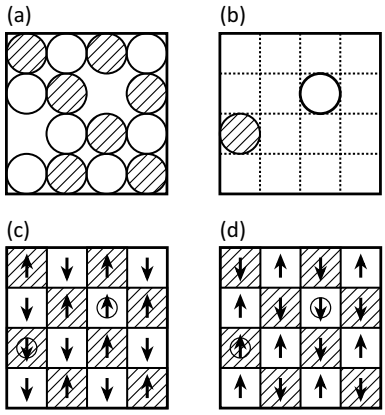

Figure 3. The Ising model and lattice gas model. (a) A surface configuration. The striped particles indicate B-particles. (b) Another surface configuration with the two empty sites in (a) changed to occupied sites and the occupied sites in changed to empty sites. (c) Spin configuration corresponding to (a). The open areas and striped areas denote $\mathcal{A}'$ sub-lattice sites and $\mathcal{B}'$ sub-lattice sites, respectively. The circled spins are flipped from the antiferromagnetic order. (d) Spin configuration corresponding to (b). The energy of this spin configuration is the same as the energy of the spin configuration in (c).

Since the crystal surface is a 2D object, the thermal fluctuations are sometimes strong enough to destroy the ordered state [23]. Because of this, mean field (or quasi chemical) calculations with respect to phase transitions may give incorrect results. To obtain reliable thermodynamic results including phase transitions, we use the PWFRG method [4, 5, 6], which is a transfer matrix version of the DMRG method [1, 2, 3]. To more easily perform the PWFRG calculations, the 2D lattice gas models are mapped to the equivalent 2D Ising model.

For the (0001) surface, we introduce the Ising spin variables $\sigma_{\mathcal{A}'}(\vec{x}) = \{1, -1\}$ and $\sigma_{\mathcal{B}'}(\vec{x}) = \{-1, 1\}$, as (Fig. 3)

$$C_{\mathcal{A}'}(\vec{x}) = \frac{1}{2}\left(\sigma_{\mathcal{A}'}(\vec{x}) + 1\right), \quad C_{\mathcal{B}'}(\vec{x}) = \frac{1}{2}\left(1 - \sigma_{\mathcal{B}'}(\vec{x})\right). \tag{9}$$

Substituting Eq. (9) into the lattice gas Hamiltonian Eq. (1), at the equilibrium we have the spin Hamiltonian

$$\begin{aligned}
\mathcal{H}_{s,b} &= J\sum_{(\vec{x})}[\sigma_{\mathcal{A}'}(\vec{x})\sigma_{\mathcal{B}'}(\vec{x}) + \sigma_{\mathcal{A}'}(\vec{x})\sigma_{\mathcal{B}'}(\vec{x} - \vec{b}) \\
&\quad + \sigma_{\mathcal{A}'}(\vec{x})\sigma_{\mathcal{B}'}(\vec{x} - \vec{b} - \vec{a})] \\
&\quad - H\sum_{\vec{x}}[\sigma_{\mathcal{A}'}(\vec{x}] + \sigma_{\mathcal{B}'}(\vec{x})) + \text{constant}, \qquad (10) \\
&\quad J = \phi/4, \quad H = (\Delta\mu_A + \Delta E_b)/2, \qquad (11)
\end{aligned}$$

where J is the anti-ferromagnetic coupling constant between nn spins and H is the uniform magnetic field.

Similarly, for the prism plane, we obtain the following spin Hamiltonian from the lattice gas Hamiltonian Eq. (2):

$$\begin{aligned}
\mathcal{H}_{s,p} &= J\sum_{(\vec{x})}[\sigma_{\mathcal{A}'}(\vec{x})\sigma_{\mathcal{B}'}(\vec{x}) + \sigma_{\mathcal{A}'}(\vec{x})\sigma_{\mathcal{B}''}(\vec{x} - \vec{b}) \\
&\quad + \sigma_{\mathcal{A}'}(\vec{x})\sigma_{\mathcal{B}''}(\vec{x} - \vec{b} - \vec{a}) + \sigma_{\mathcal{A}''}(\vec{x})\sigma_{\mathcal{B}'}(\vec{x}) \\
&\quad + \sigma_{\mathcal{A}''}(\vec{x})\sigma_{\mathcal{B}''}(\vec{x}) + \sigma_{\mathcal{A}''}(\vec{x})\sigma_{\mathcal{B}'}(\vec{x} + \vec{a})] \\
&\quad - H\sum_{\vec{x}}[\sigma_{\mathcal{A}'}(\vec{x}) + \sigma_{\mathcal{B}'}(\vec{x}) + \sigma_{\mathcal{A}''}(\vec{x}) + \sigma_{\mathcal{B}''}(\vec{x})] \\
&\quad - H_{\text{st}}\sum_{\vec{x}}[\sigma_{\mathcal{A}'}(\vec{x}) - \sigma_{\mathcal{B}'}(\vec{x}) - \sigma_{\mathcal{A}''}(\vec{x}) + \sigma_{\mathcal{B}''}(\vec{x})] \\
&\quad + \text{constant}, \qquad (12)
\end{aligned}$$

where

$$J = \phi/4, \quad H = \Delta\mu_A/2, \quad H_{st} = \Delta E_p/2. \tag{13}$$

Here, H_{st} is a staggered field connected to the bond vertical to the prism plane.

3. PRODUCT-WAVE-FUNCTION RENORMALIZATION-GROUP ALGORITHM

3.1. Transfer Matrix for a Finite System

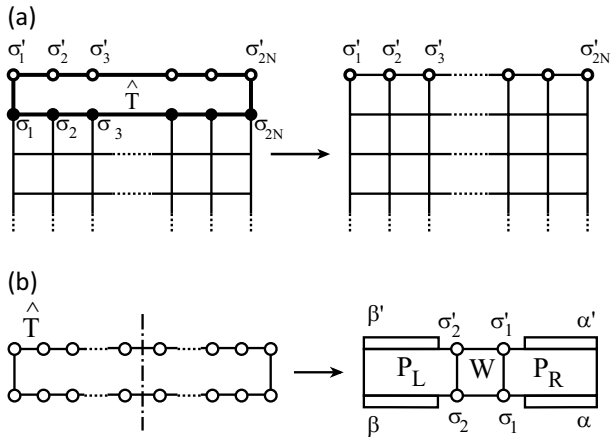

Figure 4. Operation of transfer matrix. (a) The number of rows r on the left system increases to $r+1$ on the right system by the operation of the transfer matrix on the planar system. The closed circles indicate summation with respect to $\{\sigma_i\}$. (b) The right and the left transfer matrices P_R and P_L. W indicates the elementary transfer matrix connecting P_R and P_L.

We now explain how to apply the DMRG method to the surface system. More rigorously, we adopt the PWFRG method.

Let us consider that one axis of the 2D classical Ising system indicates imaginary time and the other axis shows the location of the 1D system. Then, the transfer matrix connecting a horizontal row to a neighboring horizontal row works as the connectivity matrix from imaginary time it to $i(t+\Delta t)$, where $i^2=-1$, for the 1D quantum system [30, 31, 32]. As shown in Fig. 4, in an $M\times 2N$ Ising model with nn interactions, a row of spins $\{\sigma_i\}$ is connected to the next row of spins $\{\sigma_i'\}$ by the row to row transfer matrix $\hat{T}$ as follows:

$$|\tilde{\psi}'(\sigma_1',\sigma_2',\cdots,\sigma_{2N}')>=\hat{T}|\tilde{\psi}(\sigma_1,\sigma_2,\cdots,\sigma_{2N})>, \tag{14}$$

where $2N$ is the number of spins in a row. $\hat{T}$ is a $q^{2N}\times q^{2N}$ matrix, where $q=2$ is the freedom of a spin. There are no occupied states to the left of the spin at

σ_1 or to the right of σ_{2N}. In the thermodynamic limit, the partition function Z of the 2D classical system is given by

$$Z = \lim_{N,M\to\infty} \mathrm{Tr}\, \hat{T}^M = \lim_{N,M\to\infty} \lambda_{\max}^M, \tag{15}$$

where $\lambda_{\max}$ is the maximum eigenvalue of the transfer matrix. The free energy density of the system $f(T)$ is obtained by

$$f(T) = \lim_{N,M\to\infty} \frac{1}{2N} \ln \lambda_{\max}. \tag{16}$$

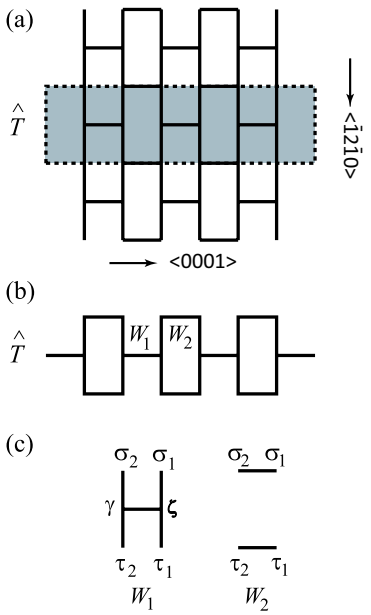

Figure 5. (a) Transfer matrix for the Ising model modeled on the $(10\bar{1}0)$ surface of the wurtzite crystal structure. (b) Intra structure of the transfer matrix. (c) Spin configuration for the elemental matrices for the transfer matrix.

In a finite size system, an approximate value λ of the maximum eigenvalue and its wave-function is obtained by

$$\lambda = \langle\psi|\hat{T}|\psi\rangle / \langle\psi|\psi\rangle. \tag{17}$$

To apply the DMRG algorithm, we divide the finite-size transfer matrix into a right transfer matrix P_R, left transfer matrix P_L, and elementary transfer matrix W (Fig. 4 (b)). Here, the size of P_R (or P_L) is $(q \times m) \times (q \times m)$ with m. Using the right and left transfer matrices, the transfer matrix is expressed as

$$\hat{T} = P_L(\sigma_2', \beta'; \sigma_2, \beta) W(\sigma_2', \sigma_1'; \sigma_2, \sigma_1) P_R(\sigma_1', \alpha'; \sigma_1, \alpha). \tag{18}$$

Here, α, α', β, and β' denote the *block spin* indexes, which run from 1 to m.

We now introduce the transfer matrix for the wurtzite Ising model Eqs. (10) and (12). Two kinds of elemental transfer matrices W_1 and W_2, which appear alternately, are introduced (Fig. 5). The explicit form of the matrices are

$$\begin{aligned}
W_1 &= \sum_{\{\alpha\},\{\gamma\}} \exp[-\mathcal{H}_1/k_{\rm B}T], && (19)\\
\mathcal{H}_1 &= J[\tau_1\zeta + \zeta\sigma_1 + \zeta\gamma + \tau_2\gamma + \gamma\sigma_2] \\
&\quad -\frac{H_{\rm st}}{4}(\tau_1 + 4\zeta + \sigma_1 - \tau_2 - 4\gamma - \sigma_2) \\
&\quad -\frac{H}{4}(\tau_1 + 4\zeta + \sigma_1 + \tau_2 + 4\gamma + \sigma_2), && (20)\\
W_2 &= \exp[-\mathcal{H}_2/k_{\rm B}T], && (21)\\
\mathcal{H}_2 &= \frac{J}{2}[\tau_1\tau_2 + \sigma_1\sigma_2] - \frac{H_{\rm st}}{4}(-\tau_1 - \sigma_1 + \tau_2 + \sigma_2) \\
&\quad -\frac{H}{4}(\tau_1 + \sigma_1 + \tau_2 + \sigma_2), && (22)
\end{aligned}$$

where $k_{\rm B}$ is the Boltzmann constant, T is the temperature, and σ_i, τ_i, γ, and ζ are spins. It should be noted that $P_{\rm R}$ is not identical to $P_{\rm L}$ due to the lack of inversion symmetry.

3.2. Density Matrix

Let us denote the wave-function of the transfer matrix using the block spins, such as $\psi(\beta, \sigma_2; \sigma_1, \alpha)$ (Fig. 6 (a)).

The right density matrix $\rho_{\rm R}(\sigma'', \gamma; \sigma, \alpha)$ and left density matrix $\rho_{\rm L}(\sigma'', \gamma; \sigma, \alpha)$ are defined by the following equations, as illustrated in Fig. 6 (b) and (c):

$$\begin{aligned}
\rho_{\rm R}(\sigma'', \gamma; \sigma, \alpha) &= \sum_{\{\sigma'\},\{\beta\}} \psi^t(\gamma, \sigma''; \sigma', \beta)\psi(\beta, \sigma'; \sigma, \alpha), && (23)\\
\rho_{\rm L}(\sigma'', \gamma; \sigma, \alpha) &= \sum_{\{\sigma'\},\{\beta\}} \psi^t(\sigma', \beta; \gamma, \sigma'')\psi(\sigma, \alpha; \beta, \sigma'), && (24)
\end{aligned}$$

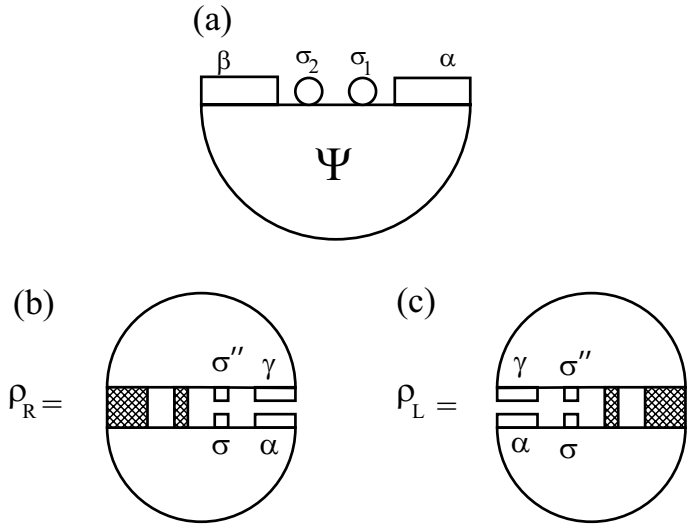

Figure 6. Diagrammatic representation of the wave function and density matrices. (a) Wave function. (b) Right density matrix. (c) Left density matrix. The shaded indexes represent the sum with respect to the block spins or the spin.

and the density matrix satisfies

$$\mathrm{Tr}\rho_{\mathrm{R}} = \mathrm{Tr}\rho_{\mathrm{L}} = 1. \tag{25}$$

Since the wurtzite Ising AF does not have inversion symmetry, we have $\rho_{\mathrm{R}} \neq \rho_{\mathrm{L}}$.

3.3. Sublattice Magnetizations

The sublattice magnetizations of the sites σ_1 and σ_2, which appear in W_2, are obtained as

$$m_{\mathcal{B}'} = \langle\sigma_1\rangle = \langle\psi'|\hat{\sigma_1}\delta_K(\sigma_1,\tau_1)\delta_K(\sigma_2,\tau_2)|\psi'\rangle, \tag{26}$$
$$m_{\mathcal{A}'} = \langle\sigma_2\rangle = \langle\psi'|\hat{\sigma_2}\delta_K(\sigma_1,\tau_1)\delta_K(\sigma_2,\tau_2)|\psi'\rangle, \tag{27}$$

where $|\psi'\rangle$ is $\hat{T}|\psi\rangle/\sqrt{\langle\psi''|\psi''\rangle}$ and $|\psi''\rangle = \hat{T}|\psi\rangle$. To obtain the values for the sites α and γ, we define the sublattice magnetization operators $\hat{M_\alpha}$ and $\hat{M_\gamma}$ as

$$\hat{M_\alpha} = \sum_{\{\alpha\},\{\gamma\}} \alpha \exp[-\mathcal{H}_1/k_{\rm B}T], \tag{28}$$

$$\hat{M_\gamma} = \sum_{\{\alpha\},\{\gamma\}} \exp[-\mathcal{H}_1/k_{\rm B}T]\gamma. \tag{29}$$

Then, the expectation values are obtained as

$$m_{\mathcal{B}''} = \langle M_\alpha \rangle = \frac{\langle\psi|P_{\rm L}\hat{M}_\alpha P_{\rm R}|\psi\rangle}{\langle\psi|P_{\rm L}\hat{W}_1 P_{\rm R}|\psi\rangle}, \tag{30}$$

$$m_{\mathcal{A}''} = \langle M_\gamma \rangle = \frac{\langle\psi|P_{\rm L}\hat{M}_\gamma P_{\rm R}|\psi\rangle}{\langle\psi|P_{\rm L}\hat{W}_1 P_{\rm R}|\psi\rangle}. \tag{31}$$

The internal energy per unit cell $E = E_1 + E_2$ is obtained as follows:

$$E_2 = \langle\mathcal{H}_2\rangle = \langle\psi'|\mathcal{H}_2\delta_K(\sigma_1,\tau_1)\delta_K(\sigma_2,\tau_2)|\psi'\rangle, \tag{32}$$

$$E_1 = \frac{<\psi|P_{\rm L}\hat{H}_1 P_{\rm R}|\psi>}{<\psi|P_{\rm L}\hat{W}_1 P_{\rm R}|\psi>}, \tag{33}$$

where

$$\hat{H}_1 = \mathcal{H}_1 \exp[-\mathcal{H}_1/k_{\rm B}T]. \tag{34}$$

The specific heat is calculated as $\delta E/\delta T$, where $\delta E = E(T+\delta T) - E(T)$.

3.4. Renormalization

In this subsection, the PWFRG iteration is outlined briefly.

First, the elementary transfer matrices W_1 and W_2 are calculated. Then, the initial right and left block transfer matrices $P_{\rm R}$ and $P_{\rm L}$ are prepared using W_1. Next, an initial wave-function vector ψ is prepared. Then, the iteration is started.

1. $P_{\rm R}$, $P_{\rm L}$, and W_i are operated on the wave-function vector to produce Ψ'' and Ψ' (Fig. 7 (a)). If the iteration time is odd, $W_i = W_1$, otherwise $W_i = W_2$. The operation is repeated i_{mp} times where $i_{mp} = 3$ in the present calculations.

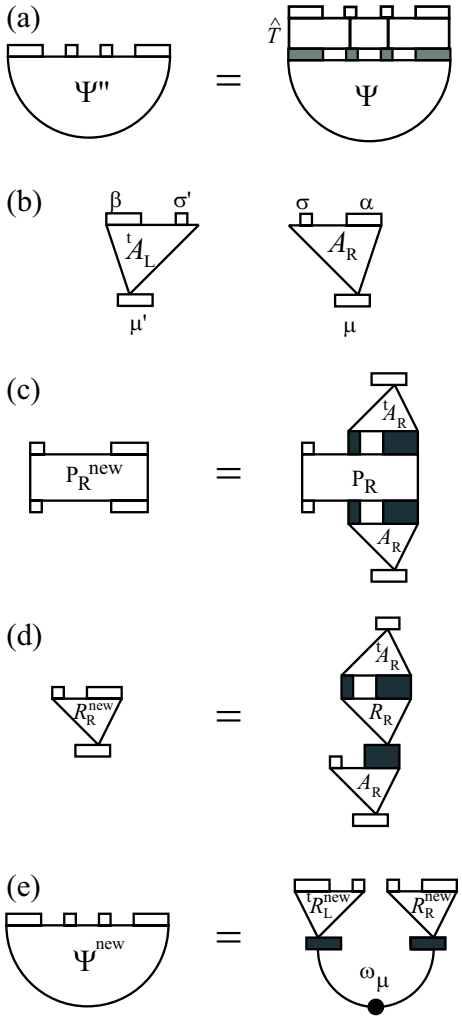

Figure 7. Diagrammatic representations of the PWFRG iteration, where the shaded parts denote summations over the bases. (a) Wave-function vector after operation of the transfer matrix on the old wave-function vector. (b) Right and left contraction matrices. (c) Update of the right transfer matrix. (d) Update of the right wave-function matrix. (e) New wave-function vector produced by the wave-function matrices.

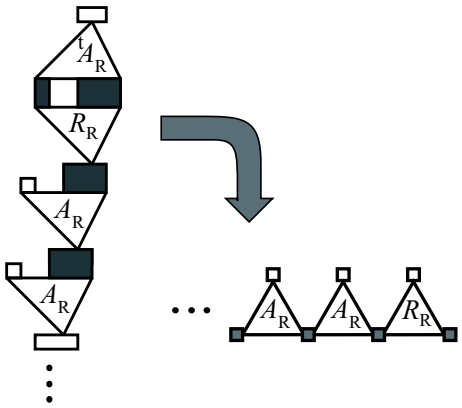

Figure 8. Diagrammatic expression of the wave function being updated by the iterative product of the contraction matrices.

2. The physical quantities, such as the sub-lattice magnetizations and the value of the partition function, are calculated using Ψ'.

3. The wave-function vector Ψ' is decomposed into the right and left wave-function matrices R_R and R_L with a size of $(q \times m) \times (q \times m)$.

4. The right and left density matrices ρ_R and ρ_L (Fig. 6 (b) and (c)) are calculated using Ψ'.

5. The eigenvalues $\{\omega_\mu\}$ and eigenvectors of the right and left density matrices ρ_R and ρ_L are calculated. The eigenvectors are sorted in decreasing order of eigenvalue. The size of the matrix formed by the eigenvectors is $(q \times m) \times (q \times m)$. The right and left contraction matrices A_R and A_L are obtained by discarding the eigenvectors with eigenvalues smaller than the m-th eigenvalue (Fig. 7 (b)). The size of the contraction matrices is reduced to $(q \times m) \times m$.

6. The elementary transfer matrix W_i is added to the right transfer matrix P_R. The size of the resultant P_R is $(q^2 \times m) \times (q^2 \times m)$. Using the right contraction matrix A_R, the size of P_R is reduced to give $P_R^{\rm new}$ (Fig. 7 (c)). A similar operation is performed on the left transfer matrix P_L to obtain $P_L^{\rm new}$.

7. The new right wave-function matrix $R_R^{\rm new}$ is obtained by operating A_R to obtain R_R (Fig. 7 (d)). A similar operation is performed on the left wave-function matrix R_L to obtain $R_L^{\rm new}$.

8. The new wave-function vector $\Psi^{\rm new}$ is calculated using $R_R^{\rm new}$ and $R_L^{\rm new}$ (Fig. 7 (e)).

9. Return to 1. The iteration is repeated until the max-iteration value is reached.

The iterative operation of the transfer matrix in step 1 is key to this method and gradually leads the maximum-eigenvalue wave function. Also important is the contraction of the bases according to the eigenvalues of the density matrix, after they were increased by the addition of another W_i to the transfer matrix. Owing to these principles, the important bases for the maximum-eigenvalue wave function are not discarded. The wave function converges to the maximum-eigenvalue wave function efficiently.

Although the number of bases for the "block spin" m is not large, the approximate values of the physical quantities in the present method are more reliable than the mean field approximation because the contraction matrix is multiplied over each iteration to obtain the product-wave-function for the larger system size (Fig. 8). Therefore, after sufficient iterations, we obtain values of the physical quantities for a sufficiently large system size.

4. RESULTS

At $H = 0$ and $H_{\rm st} = 0$, the Ising model Eqs (10) and (12) reduce to the exactly solvable honeycomb Ising AF. The known exact transition temperature is $k_{\rm B}T_{\rm N}/J = 2/[\ln(2+\sqrt{3})] \approx 1.5186514$ obtained from $\cosh[2J/(k_{\rm B}T_{\rm N})] = 2$ [33]. For the PWFRG calculation, the number of bases is $m = 4$–12, and the maximum number of iterations is 400–50,000. Near to the transition temperature, a greater number of bases and iterations are required to obtain precise values. The transition temperature obtained at the zeros of the magnetization calculated by the PWFRG was $k_{\rm B}T_{\rm N}^{(m)}/J = 1.5188$, where the critical exponent $\beta = 1/8$ for the 2D Ising model is assumed. The transition temperature obtained by the specific heat calculated by the PWFRG method was $k_{\rm B}T_{\rm N}^{(c)}/J = 1.5185$ assuming logarithmic behavior of the specific heat (Fig. 9). Thus, the errors of $T_{\rm N}^{(m)}$ and $T_{\rm N}^{(c)}$ are less than 100 ppm.

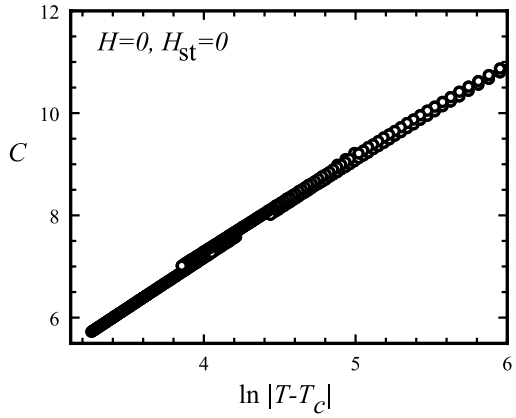

Figure 9. Logarithmic behavior of the specific heat calculated by PWFRG. $H = 0$, $H_{\rm st} = 0$, $k_{\rm B}T_{\rm N}^{(c)}/J = 1.5185$.

For $H_{\rm st} = 0$ and $H/J = \Delta E_b/(2J) \approx 1$, the Ising model Eqs. (10) and (12) express the one-component lattice gas model of the (0001) surface of the wurtzite structure or the (111) surface of the cubic zinc-blend structure. Examples of the surface are the basal plane of Ih–ice and the (111) surface of Si. At $H/J = 1$, the calculated transition temperature was

$$k_{\rm B}T_{\rm N}^{(0001)}/J = 1.3871. \tag{35}$$

For $H = 0$ and $H_{st}/J = \Delta E_p/(2J) \approx 1$, the Ising model Eq. (12) expresses the one-component lattice gas on the prism surface of the wurtzite crystal structure. The temperature dependence of the sublattice magnetization is shown in Fig. 10 (a). The PWFRG results are shown by lines and the Monte Carlo (MC) results with the Metropolis algorithm are shown by symbols, where the linear size of the MC system is 32–128, and the average time is 1×10^6 MC-step per site. Both results agree well.

Let us introduce sub-lattice order parameters as

$$q = |\sigma_{\mathcal{A}'} - \sigma_{\mathcal{B}''}|, \tag{36}$$
$$q' = |\sigma_{\mathcal{A}''} - \sigma_{\mathcal{B}'}|. \tag{37}$$

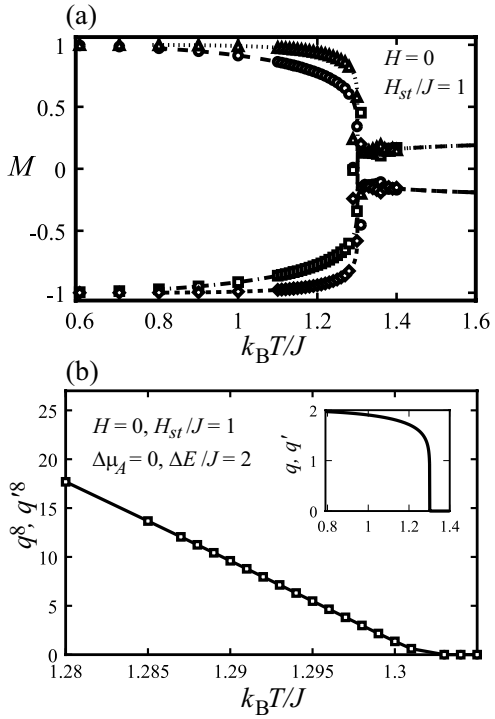

Figure 10. (a) Temperature dependence of the sublattice magnetization. The dashed lines denote PWFRG calculations ($\mathcal{A}'$ long dashed line, $\mathcal{A}''$ dotted line, $\mathcal{B}'$ dotted dashed line, and $\mathcal{B}''$ short dashed line). The open circles, open squares, open triangles, and open diamonds show MC calculations. (b) Temperature dependence of the order parameters to the 8-th power. From the extrapolation of the line to $q^b = 0$, we obtain $k_{\rm B}T_{\rm N}^{(m)}/J = 1.3015$. The inset graph shows the temperature dependence of the order parameters.

We do not normalize them to 1. The temperature dependence of the order parameters are shown by the inset figure in Fig. 10 (b). Based on the critical exponent of the order parameter $\beta = 1/8$ for the 2D Ising model, the temperature dependence of q^8 and q'^8 are shown in Fig. 10 (b). As seen from the figure, q^8 agrees well with q'^8 and decreases linearly. By extrapolating the line

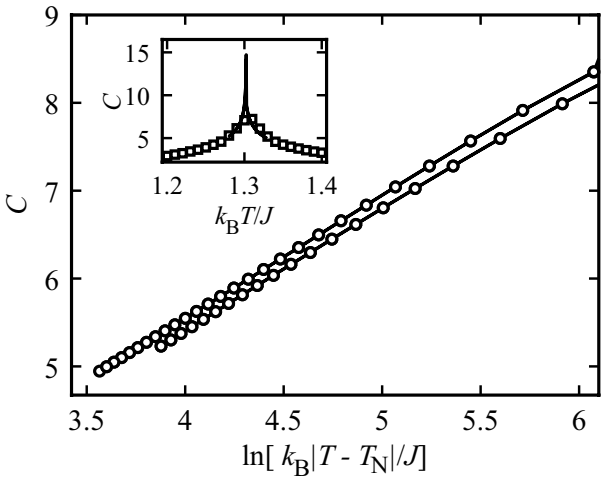

Figure 11. Logarithmic behavior of the specific heat. $k_{\rm B}T_{\rm N}^{(c)}/J = 1.3012$, $H = 0$, $H_{\rm st}/J = \Delta E_p/(2J) = 1$. The open circles show the values obtained by the PWFRG calculation. The lines connect neighboring circles. The inset shows the temperature dependence of the specific heat. The solid line shows the values obtained by the PWFRG calculations while the open squares show the MC calculation (64×64).

to $q, q' = 0$, the transition temperature is obtained as

$$k_{\rm B}T_{\rm N}^{(m)}/J = 1.3015. \tag{38}$$

The calculated specific heat values are shown in Fig. 11. The lines calculated by the PWFRG method show a sharp peak, whereas the values calculated by the MC method show a low peak due to the finite size effect. From the semi-logarithmic figure of the specific heat, the transition temperature is obtained as

$$k_{\rm B}T_{\rm N}^{(c)}/J = 1.3012. \tag{39}$$

To obtain this value, the critical amplitude at temperatures higher than $T_{\rm N}$ is assumed to be the same as the critical amplitude at temperatures lower than $T_{\rm N}$. $k_{\rm B}T_{\rm N}^{(c)}/J = 1.3012$ agrees well with $k_{\rm B}T_{\rm N}^{(m)}/J = 1.3015$.

5. APPLICATION TO IH–ICE

Table 1. Microscopic quantities($a = 4.52$ Å, $c = 7.36$ Å)

Quantity	Equation	Value	
	Ice/vapor interface	Ice/water interface	
$T_{R,b}$	$\geq T_{\rm N}^{(0001)}$	289 K	274 K
$T_{R,p}$	$\geq T_{\rm N}^{(10\bar{1}0)}$	271 K [38]–[42]	257 K [69, 70]
$\phi_b \approx \phi_p$	$4J$	71.8 meV	68.1 meV
$\Delta E_b \approx \Delta E_p$	$2H = \phi_b/2$	35.9 meV	34.0 meV
$\gamma_{\rm surf}^{(0001)}$	$T = 0$ K	32.5 mJ/m^2	30.8 mJ/m^2
$\gamma_{\rm surf}^{(10\bar{1}0)}$	$T = 0$ K	34.6 mJ/m^2	32.8 mJ/m^2

5.1. The Ice/Vapor Surface

Usually, crystal/vapor interfaces (surfaces) are thought to be well defined. However, in the case of the Ih–ice/vapor surface, the surface structure is complex because the metastable quasi-liquid layer (QLL) [35]–[48] exists on the ice surface.

While a recent simulation study [49] showed that ice-like molecules can be distinguished from liquid-like molecules locally by using a tetrahedral order parameter [50, 51]. In addition, from detailed ice/QLL interface laser confocal microscopy observations combined with differential interference contrast microscopy (LCM-DIM) [52], kinks and steps are observed on the surface between the ice and the QLL [53].

The efficacy of the tetrahedral order parameter suggests the difference between ice and liquid is not due to the behavior of the long-range order but the behavior of the 3D Ising model. Hence, we assume that the lattice gas model is effective for the ice/QLL or ice/vapor surface. The surface energy of a surface configuration is calculated using the lattice gas Hamiltonian Eqs. (1) and (2) based on the number of broken bonds.

To obtain the effective bond energy, we start from the faceting transition temperature at the prism surface [38]–[42]. The faceting transition temperature is the same as the roughening transition temperature of the surface [54]–[60]. It

should be noted that the transition temperature of the 2D Ising system gives a lower limit of the roughening transition temperature. This is because the roughening transition is caused by the proliferation of surface steps where the step free-energy is equal to zero. Self-similarly formed islands or holes due to thermal fluctuations pin the zig-zag configurations at a step-edge temporally. The pinning of the step configurations decreases the step entropy. In the lattice gas system, these islands or holes do not pin the steps (interfaces). Hence to reduce the step free energy to zero, a higher temperature than that of the Ising model is required.

The faceting transition temperature on the prism plane is observed at about 271–272 [K].[38]–[42] Therefore, we adopt the phase transition temperature of the $(10\bar{1}0)$ surface as -2 [°C]. From Eq. (39), with $T_{\rm N}^{(10\bar{1}0)} = 271$ [K], $2J$ is obtained as 35.89 [meV]. Assuming $\phi_b = \phi_p$ with Eq. (35), we obtain $T_{\rm N}^{(0001)} = 289$ [K]. This temperature is higher than the melting temperature of ice, which is consistent with the experiments. Using the value of ϕ_p, the surface tension at $T = 0$ [K] is also obtained.

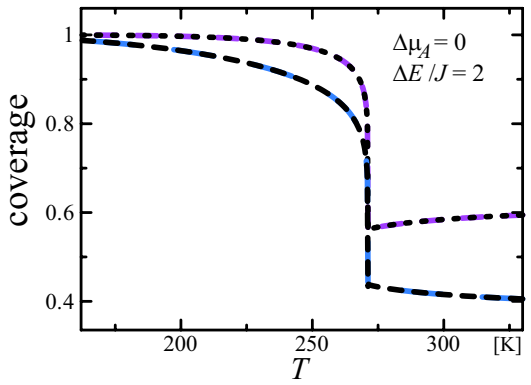

Figure 12. Temperature dependence of the coverage of the $(10\bar{1}0)$ surface for the ice/vapor interface. Dotted line: $\mathcal{A}'$ sub-lattice site. Dashed line (red): $\mathcal{B}'$ sub-lattice site. Short dashed line: $\mathcal{A}''$ sub-lattice site. Long dashed line (blue): $\mathcal{B}''$ sub-lattice site.

Fig. 12 shows the coverages of the sub-lattice sites calculated with the sub-lattice magnetization obtained by the PWFRG method. From the figure, we can see that the molecules on the $\mathcal{A}'$ and $\mathcal{B}'$ sub-lattice sites are more stable than

the molecules on the $\mathcal{A}''$ and $\mathcal{B}''$ sub-lattice sites at all temperatures. Since the molecules on the $\mathcal{A}''$ and $\mathcal{B}''$ sub-lattice sites have dangling bonds ΔE_p that protrude from the surface, the results are plausible. The microscopic quantities are summarized in Table **??**. The obtained results lie in the range of the experimentally obtained values.

5.2. The Ice/Water Interface

The interface tension of Ih–ice/water $\gamma_{\rm SL}$ can be measured by the nucleation [61, 62], equilibrium contact angle [63], and equilibrium shape of ice grain boundary grooves [64]–[68]. The values of $\gamma_{\rm SL}$ lie between 25–41 [mJ/m^2].

Recently, measurements of the roughening transition of the $(10\bar{1}0)$ plane on Ih–ice in water under 165 [Mpa] have been reported.[69, 70] They faceting transition was observed optically and the crystal growth mode was studied, *i. e.* the nucleation growth mode and step growth with screw dislocation. It was concluded that the roughening transition temperature of the prism plane is -16 [$^\circ$C]. We adopt Maruyama's roughening transition temperature as the present $T_{\rm R}$ ($\approx T_{\rm N}$).

Using this $T_{\rm N}^{(10\bar{1}0)}$ for the prism plane, we obtained $T_{\rm N}^{(0001)}$, which is slightly above the melting temperature of ice at 1 atm, by assuming $\phi_p = \phi_b = 2\Delta E_p = 2\Delta E_b$. The microscopic quantities ϕ_b and ϕ_p are summarized in Table **??**. The estimated ice/water surface energies $\gamma_{\rm surf}^{(10\bar{1}0)}$ and $\gamma_{\rm surf}^{(0001)}$ at $T = 0$ K also lie in the region of the experimentally observed values [61]–[68]. The present $\gamma_{\rm surf}^{(0001)}$ also agrees well with the results obtained by the recent molecular dynamic calculations [71, 72].

The sub-lattice coverage is similar to Fig. 12. The difference is the values of the effective bonds ϕ_p.

6. DISCUSSION

We neglect the second nn coupling between A–A or B–B particles. The difference between A particles and B particles, such as Si atoms and C atoms [73], are not taken into consideration. For a two-component system, the sub-lattice coverage and the phase transition temperature depend on the temperature T and the relative chemical potential $\Delta\mu_A$ in the ambient phase. The T and $\Delta\mu_A$ dependent results are the out of the scope of this article and will be presented elsewhere.

In the case of the PWFRG calculations for the RSOS family models, the transfer matrix is constructed by a combination of the vertices [15, 10, 34]. In particular, i_{mp} should be about 90 to obtain convergent values in the iteration. This may be because there are a large number of states near the ground state.

Since the phase transition temperature of the 2D lattice gas model is lower than the true roughening transition temperature, the values of the effective bonds should be smaller than the present values. Also, although the value of the surface tension for a smooth surface is almost constant, the surface tension at a finite temperature decreases near the faceting transition as the temperature increases due to the increase of the entropy with respect to the variety of surface configurations. This explains why our values are slightly larger than the values obtained by Benet *et al.* [74] for the surface stiffness [59, 74].

Acknowledgments

The author wishes to acknowledge Mr. T. Matsui and Mr. R. Oku for checking the Monte Carlo program, and producing several of the results. The author thanks Professor G. Sazaki and Professor Y. Furukawa for continual encouragement for the study on ice. This work was supported by a Grant-in-Aid for Scientific Research from the Ministry of Education, Science and Culture (No. 07640521). This work was also supported by KAKENHI Grants-in-Aid (nos. JP25400413 and JP17K05503) from the Japan Society for the Promotion of Science (JSPS). A part of the numerical computations was made on the system VPP500 of the Supercomputer Center, Institute for Solid State Physics, the University of Tokyo.

CONCLUSION

For the two-dimensional (2D) lattice gas model on the (0001) and $(10\bar{1}0)$ surfaces of a wurtzite crystal struacture, reliable phase transition temperatures $T_{\rm N}^{(0001)}$ and $T_{\rm N}^{(10\bar{1}0)}$ were calculated using the PWFRG method.

- For the case of an nn honeycomb Ising model ($\Delta\mu_A = 0$ and $\Delta E_b = 0$ or $H = 0$ and $H_{st} = 0$), the obtained transition temperature $k_{\rm B}T_{\rm N}^{(m)}/J = 1.5188$ used in the PWFRG method agrees with the exact value of $k_{\rm B}T_{\rm N}/J) = 2/[\ln(2+\sqrt{3})] \approx 1.5186514$, giving an error of less than 100 ppm. In the case of the lattice gas on the basal plane ($\Delta E_b/(2J) = 1$ and

$\Delta\mu_A = 0$ in Eq. (11)), the transition temperature $k_{\rm B}T_{\rm N}^{(0001)}/J = 1.3871$ is obtained. In the case of the lattice gas on the prism plane ($\Delta E_p/(2J) = 1$ and $\Delta\mu_A = 0$ in Eq. (13)), $k_{\rm B}T_{\rm N}^{(m)}/J = 1.3015$ is obtained.

- For Ih–ice, the effective bond energy ϕ_p for the ice/vapor and the ice/water prism surfaces (interfaces) were obtained as 71.8 meV and 68.1 meV, respectively, by a comparison with the experimental values of the faceting transition temperatures. Here, the faceting transition temperature is approximated by the phase transition temperature of the 2D lattice gas model.

- Assuming $\phi_p = \phi_b = 2\Delta E_b = 2\Delta E_p$, the ice/vapor surface (interface) energies at $T = 0$ K were estimated for both the (0001) and $(10\bar{1}0)$ surfaces, $\gamma_{\rm surf}^{(0001)}$ and $\gamma_{\rm surf}^{(10\bar{1}0)}$, obtained as 32.5 mJ/m^2 and 34.6 mJ/m^2, respectively (Table 1). The surface energies of the ice/water surface $\gamma_{\rm surf}^{(0001)}$ and $\gamma_{\rm surf}^{(10\bar{1}0)}$ are also obtained as 30.8 mJ/m^2 and 32.8 mJ/m^2, respectively.

REFERENCES

[1] White S. R., "Density matrix formulation for quantum renormalization groups", *Phys. Rev. Lett.*, **69**, 2863–2866 (1992).

[2] Nishino T., "Density matrix renormalization group method for 2D classical models", *J. Phys. Soc. Jpn.*, **64**, 3598–3601 (1995).

[3] Schollwöck U., "The density-matrix renormalization group", *Rev. Mod. Phys.*, **77**, 259–315 (2005).

[4] Nishino T., Okunishi K., "Product wave function renormalization group", *J. Phys. Soc. Jpn.*, **64**, 4084–4087 (1995).

[5] Hieida Y., Okunishi K. and Akutsu Y., "Magnetization process of a one-dimensional quantum antiferromagnet: The product-wave-function renormalization group approach", *Phys. Lett. A*, **233**, 464–470 (1997).

[6] Hieida Y., Okunishi K. and Akutsu Y., "Numerical renormalization approach to two-dimensional quantum antiferromagnets with valence-bond-solid type ground state", *New J. Phys.*, **1**, 7 (1999).

[7] Suzuki M., "Generalized Trotter's Formula and Systematic Approximants of Exponential Operators and Inner Derivations with Applications to Many-Body Problems", *Comm. Math. Phys. 51, (1976) 183–190*; H. F. Trotter, "On the product of semi-groups of operators", *Proc. of the American Math. Soc.* 10, (1959) 545–551.

[8] Akutsu N. and Akutsu Y., "Thermal evolution of step stiffness on the Si (001) surface: Temperature-rescaled Ising-model approach", *Phys. Rev. B*, **57**, R4233–R4236 (1998).

[9] Akutsu N. and Akutsu Y.,"Trimer-Monomer Mixture Problem on (111) 1×1 Surface of Diamond Structure", *Prog. Theor. Phys.* **105** 123–130 (2001).

[10] Akutsu N., Akutsu Y., and Yamamoto T., "Stiffening transition in vicinal surfaces with adsorption", *Prog. Theory Phys.*, **105**, 361–366 (2001).

[11] Akutsu N., Akutsu Y. and Yamamoto T., "Statistical mechanics of the vicinal surfaces with adsorption", *Surf. Sci.* **493**/1-3, 475–476 (2001).

[12] Akutsu N., Akutsu Y. and Yamamoto T., "Thermal step bunching and interstep attraction on the vicinal surface with adsorption", *Phys. Rev. B* **67**, 125407, 1–15, (2003).

[13] Akutsu N., H. Hibino and Yamamoto T., "A Lattice Model for Thermal Decoration and Step Bunching in Vicinal Surface with Sub-Monolayer Adsorbates", *e-J. Surf. Sci. Nanotech.* **7**, 39–44 (2009).

[14] Akutsu N., "Thermal step bunching on the restricted solid-on-solid model with point contact inter-step attractions", *Applied Surface Science*, **256**, 1205–1209 (2009).

[15] Akutsu N., " Non-universal equilibrium crystal shape results from sticky steps", *J. Phys. Condens. Matter*, **23**, 485004 (2011).

[16] Akutsu N., "Profile of a Faceted Macrostep Caused by Anomalous Surface Tension", *Adv. Condens. Matter Phys.* **2017**, Article ID 2021510 (2017).

[17] Akutsu N., "Faceting diagram for sticky steps", *AIP Adv.*, **6**, 035301 (2016).

[18] Akutsu N., "Sticky steps inhibit step motions near equilibrium", *Phys. Rev. E* **86**, 061604 (2012).

[19] Akutsu N., "Pinning of steps near equilibrium without impurities, adsorbates, or dislocations", *J. Cryst. Growth*, **401**, 72–77 (2014).

[20] Akutsu N., "Disassembly of Faceted Macrosteps in the Step Droplet Zone in Non-Equilibrium Steady State", *Crystals*, **7**, Article ID cryst7020042, (2017).

[21] Akutsu N., "Height of a faceted macrostep for sticky steps in a step-faceting zone", *Phys. Rev. Materials* **2**, 023603 (2018).

[22] Akutsu N., "Relationship Between Macrostep Height and Surface Velocity for a Reaction-Limited Crystal Growth Process", *Cryst. Growth & Des.*, **19**, 2970–2978 (2019).

[23] Mermin N. D., Wagner H., " Absence of ferromagnetism or antiferromagnetism in one-or two-dimensional isotropic Heisenberg models", *Phys. Rev. Lett.* **1966**, **17**, 1133–1136 (1966). "Erratum: Absence of ferromagnetism or antiferromagnetism in one-or two-dimensional isotropic Heisenberg models. N. D. Mermin and H. Wagner [*Phys. Rev. Letters 17*, 1133 (1966)]." *Phys. Rev. Lett.*, **17**, 1307 (1966).

[24] Akutsu N., "Equilibrium Crystal Shape of Planar Ising Antiferromagnets in External Fields", *J. Phys. Soc. Jpn.* **61**, 477–498 (1992).

[25] Akutsu N. and Akutsu Y., "Step stiffness and equilibrium island shape of Si(100) surface: statistical-mechanical calculation by the imaginary path weight random-walk method", *Surf. Sci.* **376**, 92–98 (1997).

[26] Akutsu N. and Akutsu Y., "Statistical mechanical calculation of anisotropic step stiffness of a two-dimensional hexagonal lattice-gas model with next-nearest-neighbor interactkions: application to Si(111) surface", *J. Phys.: Condens. Matter*, **11**, 6635–6652 (1999).

[27] Akutsu N., "Measurement of microscopic coupling constants between atoms on a surface: Combination of LEEM observation with lattice model analysis", *Surf. Sci.* **630**, 109-115 (2014).

[28] Akutsu N. and Akutsu Y., "Ambiguity of Anisotropic Interface Tension for Complex Crystals", *J. Phys. Soc. Jpn.* **64**, 736–756 (1995).

[29] Takata M. and Ookawa A., "On the growth mechanism of an A-B crystal" *J. Crystal Growth* **24/25**, 515–518 (1974).

[30] Akutsu Y., Akutsu N. and Yamamoto T., "Universal jump of Gaussian curvature at the facet edge of a crystal", *Phys. Rev. Lett.* **61**, 424–427 (1988).

[31] Yamamoto T., Akutsu Y. and Akutsu N., "Universal Behavior of the Equilibrium Crystal Shape near the Facet Edge. I. A Generalized Terrace-Step-Kink Model", *J. Phys. Soc. Jpn.* **57**, 453–460 (1988).

[32] Mikheev L. V. and Pokrovsky V. L., "Free-fermion solution for overall equilibrium crystal shape", *J. de Phys. I* **1**, 373–382 (1991).

[33] For example, see I. Syozi, *Phase Transitions and Critical Phenomena*, Vol. 1, ed. C. Domb and M. S. Green (Academic, London, New York 1972) pp. 270–329.

[34] Akutsu N. and Akutsu Y., "The Equilibrium Facet Shape of the Staggered Body-Centered-Cubic Solid-on-Solid Model – A Density Matrix Renormalization Group Study–", *Prog. Theor. Phys.* **116** 983–1003 (2006).

[35] Kuroda T. and Lacmann R., "Growth kinetics of ice from the vapour phase and its growth forms", *J. Cryst. Growth* **56** 189–205 (1982).

[36] Dosch H., Lied A. and Bilgram J. H., "Glancing-angle X-ray scattering studies of the premelting of ice surfaces", *Surf. Sci.*, **327**, 145–154 (1995).

[37] J. F. van der Veen, Pluis B. and A. W. D. van der Gon, *Chemistry and Physics of Solid Surfaces*, Vol.VII, ed. R. Vanselow and R. F. Howe, (Springer, Berlin, 1988) Chap. 16, p 455.

[38] Furukawa Y., Yamamoto M. and Kuroda T., "Ellipsometric study of the transition layer on the surface of an ice crystal", *J. Cryst. Growth*, **82**, 655–677 (1987).

[39] Kouchi A., Furukawa Y. and Kuroda T., "X-RAY DIFFRACTION PATTERN OF QUASI-LIQUID LAYER ON ICE CRYSTAL SURFACE", *J. de Physique*, **48**, C1-675 - C1-677 (1987).

[40] Elbaum M., "Roughening transition observed on the prism facet of ice", *Phys. Rev. Lett.* **67**, 2982–2985 (1991).

[41] Elbaum M., Lipson S. G. and Dash J. G., "Optical study of surface melting on ice", *J. Cryst. Growth*, **129**, 491–505 (1993).

[42] Furukawa Y. and Kohata S., "Temperature dependence of the growth form of negative crystal in an ice single crystal and evaporation kinetics for its surfaces", *J. Cryst. Growth*, **129**, 571–581 (1993).

[43] Nada H. and Furukawa Y., "Anisotropy in Molecular-Scaled Growth Kinetics at Ice –Water Interfaces", *J. Phys. Chem.* **B 101**, 6163-6166 (1997).

[44] Furukawa Y. and Nada H., "Anisotropic Surface Melting of an Ice Crystal and Its Relationship to Growth Forms", *J. Phys. Chem.* **B 101**, 6167-6170 (1997).

[45] Sazaki G., Zepeda S., Nakatsubo S., Yokomine M. and Furukawa Y., "Quasi-liquid layers on ice crystal surfaces are made up of two different phases", *Proc. Natl. Acad. Sci. U.S.A.* **109**, 1052–1055 (2012).

[46] Sazaki G., Asakawa H., Nagashima K., Nakatsubo S. and Furukawa Y., "How do Quasi-Liquid Layers Emerge from Ice Crystal Surfaces?", *Cryst. Growth & Design*, **13**, 1761–1766 (2013).

[47] Asakawa H., Sazaki G., Nagashima K., Nakatsubo S., and Furukawa Y., "Two types of quasi-liquid layers on ice crystals are formed kinetically", *Proc. Natl. Acad. Sci.* U.S.A. **113**, 1749–1753 (2016).

[48] Murata K., Asakawa H., Nagashima K., Furukawa Y. and Sazaki G., "Thermodynamic origin of surface melting on ice crystals", *Proc. Natl. Acad. Sci.* U.S.A. **113**, E6741–E6748 (2016).

[49] Benet J., Llombart P., Sanz E. and MacDowell L. G., "Premelting-Induced Smoothening of the Ice-Vapor Interface", *Phys. Rev. Lett.* **117**, 096101 (2016).

[50] Errington J. R. and Debenedetti P. G., "Relationship between structural order and the anomalies of liquid water", *Nature* (London) **409**, 318-321 (2001).

[51] Conde M. M., Vega C. and Ptrykiejew A., "The thickness of a liquid layer on the free surface of ice as obtained from computer simulation", *J. chem. Phys.* **129**, 014702 (2008).

[52] Sazaki G., Matsui T., Tsukamoto K., Usami N., Ujihara T., Fujiwara K., Nakajima K., *Cryst. Growth J.*, **262**, 536-542 (2004).

[53] Murata K., Nagashima K. and Sazaki G., "How Do Ice Crystals Grow inside Quasiliquid Layers?", *Phys. Rev. Lett.* **122** 026102 (2019).

[54] Jayaprakash C., Saam W. F. and Teitel S., "Roughening and facet formation in crystals", *Phys. Rev. Lett.* **50** 2017–2020 (1983).

[55] Van H. Beijeren and Nolden I., " Structure and Dynamics of Surfaces", Eds. W. Schommers, von P. Blancken-Hagen, (Springer, Berlin, Heidelberg, Germany, 1987) Volume 2, p. 259.

[56] Jayaprakash C., Rottman C. and Saam W. F., "Simple model for crystal shapes: Step-step interactions and facet edges", *Phys. Rev. B* **30**, 6549–6554 (1984).

[57] Rottman C. and Wortis M., "Equilibrium crystal shapes for lattice models with nearest- and next-nearest-neighbor interactions". *Phys. Rev. B* **29**, 328–339 (1984).

[58] Rottman C. and Wortis M., "Statistical mechanics of equilibrium crystal shapes: Interfacial phase diagrams and phase transitions", *Phys. Rep.* **103**, 59–79 (1984).

[59] Akutsu N., Akutsu Y., "Roughening, faceting and equilibrium shape of two-dimensional anisotropic interface. I. Thermodynamics of interface fluctuations and geometry of equilibrium crystal shape", *J. Phys. Soc. Jpn.*,**56**, 1443–1453 (1987).

[60] Wortis M., *Chemistry and Physics of Solid Surface VII*, Eds. R. Vanselow and R. Howe (Springer-Verlag, Berlin, Heidelberg, 1988) 367–405.

[61] Wood G. R. and Walton A. G., "Homogeneous Nucleation Kinetics of Ice from Water", *J. Appl. Phys.* **41**, 3027 (1970).

[62] Z. Zhang and X.-Y. Liu, "Contraol of ice nucleation: freezing and antifreeze strategies", *Chem. Soc. Rev.* **47**, 7116-7139 (2018).

[63] Ketcham W. M. and Hobbs P. V., "An experimental determination of the surface energies of ice", *Philos. Mag.* **19**, 1161–1173 (1969).

[64] Bolling G. F. and Tiller W. A., "Growth from the Melt. Part II. Cellular Interface Morphology", *J. Appl. Phys.* **31**, 1345 (1960).

[65] Jones D. R. H. and Chadwick G. A., "Experimental measurement of the solid-liquid interfacial energies of transparent materials", *Philos. Mag.* **22**, 291–300 (1970).

[66] Nash G. E. and Glicksman M. E., "A general method for determining solid-liquid interfacial free energies", Philos. Mag. **24** (1971) 577–592.

[67] Hardy S. C., "A grain boundary groove measurement of the surface tension between ice and water", *Philos. Mag.* **35**, 471–484 (1977).

[68] Wilen L. A. and Dash J. G., "Giant Facets at Ice Grain Boundary Grooves", *Science* **270**, 1184–1186 (1995).

[69] Maruyama M., Kishimoto Y. and Sawada T., "Optical study of roughening transition on ice Ih $(10\bar{1}0)$ planes under pressure", *J. Cryst. Growth* **172**, 521–527 (1997).

[70] M. Maruyama, "Roughening transition of prism faces of ice crystals grown from melt under pressure", *J. Cryst. Growth* **275**, 598–605 (2005).

[71] Ickes L., Welti A., Hoose C. and Lohmann U., "Classical nucleation theory of homogeneous freezing of water: thermodynamic and kinetic parameters", *J. Phys. Chem. Chem. Phys.* **17**, 5514–5537 (2015).

[72] Tanaka K. K. and Kimura Y, "Theoretical analysis of crystallization by homogeneous nuclation of water droplets", *J. Phys. Chem. Chem. Phys.* **21**, 2410–2418 (2019).

[73] Krzyzewski F. and Zaluska-Kotur M. A., "Coexistence of bunching and meandering instability in simulated growth of 4H-SiC(0001) surface", *J. Appl. Phys.* **115**, 213517 (2014).

[74] Benet J., MacDowell L. G. and Sanz E., "A study of the ice-water interface using the TIP4P/2005 water model", *Phys. Chem. Chem. Phys.* **16**, 22159–22166 (2014).